APSB

ORIGINAL ARTICLE

Discovery of a highly specific 18F-labeled PET ligand for phosphodiesterase 10A enabled by novel spirocyclic iodonium ylide radiofluorination

Zhiwei Xiao[a,b,†], Huiyi Wei[a,†], Yi Xu[c,†], Ahmed Haider[b], Junjie Wei[a], Shiyu Yuan[a], Jian Rong[b], Chunyu Zhao[b], Guocong Li[a], Weibin Zhang[d], Huangcan Chen[d], Yuefeng Li[e], Lingling Zhang[a], Jiyun Sun[a,b], Shaojuan Zhang[a], Hai-Bin Luo[f], Sen Yan[g], Qijun Cai[a], Lu Hou[a], Chao Che[d,*], Steven H. Liang[b,*], Lu Wang[a,*]

[a]Center of Cyclotron and PET Radiopharmaceuticals, Department of Nuclear Medicine and PET/CT-MRI Center, the First Affiliated Hospital of Jinan University, Guangzhou 510630, China
[b]Division of Nuclear Medicine and Molecular Imaging, Massachusetts General Hospital & Department of Radiology, Harvard Medical School, Boston, MA 02114, USA
[c]Department of Cardiology, the First Affiliated Hospital of Jinan University, Guangzhou 510630, China
[d]State Key Laboratory of Chemical Oncogenomics, Key Laboratory of Chemical Genomics, Peking University Shenzhen Graduate School, Shenzhen 518055, China
[e]Guangdong Landau Biotechnology Co. Ltd., Guangzhou 510555, China
[f]Key Laboratory of Tropical Biological Resources of Ministry of Education, School of Pharmaceutical Sciences, Hainan University, Haikou 570228, China
[g]Guangdong-Hongkong-Macau Institute of CNS Regeneration, Ministry of Education CNS Regeneration Collaborative Joint Laboratory, Jinan University, Guangzhou 510632, China

Abstract   As a member of cyclic nucleotide phosphodiesterase (PDE) enzyme family, PDE10A is in charge of the degradation of cyclic adenosine (cAMP) and guanosine monophosphates (cGMP). While PDE10A is primarily expressed in the medium spiny neurons of the striatum, it has been implicated in

*Corresponding authors. Tel./fax: +86 755 26032530 (Chao Che), +1 617 7266165 (Steven H. Liang), +86 20 38688692 (Lu Wang).

E-mail addresses: chec@pku.edu.cn (Chao Che), Liang.Steven@mgh.harvard.edu (Steven H. Liang), l_wang1009@jnu.edu.cn (Lu Wang).

[†]These authors made equal contributions to this work.

a variety of neurological disorders. Indeed, inhibition of PDE10A has proven to be of potential use for the treatment of central nervous system (CNS) pathologies caused by dysfunction of the basal ganglia—of which the striatum constitutes the largest component. A PDE10A-targeted positron emission tomography (PET) radioligand would enable a better assessment of the pathophysiologic role of PDE10A, as well as confirm the relationship between target occupancy and administered dose of a given drug candidate, thus accelerating the development of effective PDE10A inhibitors. In this study, we designed and synthesized a novel ^{18}F-aryl PDE10A PET radioligand, codenamed [^{18}F]P10A-1910 ([^{18}F]**9**), in high radiochemical yield and molar activity *via* spirocyclic iodonium ylide-mediated radiofluorination. [^{18}F]**9** possessed good *in vitro* binding affinity (IC$_{50}$ = 2.1 nmol/L) and selectivity towards PDE10A. Further, [^{18}F]**9** exhibited reasonable lipophilicity (log$D$ = 3.50) and brain permeability ($P_{app} > 10 \times 10^{-6}$ cm/s in MDCK-MDR1 cells). PET imaging studies of [^{18}F]**9** revealed high striatal uptake and excellent *in vivo* specificity with reversible tracer kinetics. Preclinical studies in rodents revealed an improved plasma and brain stability of [^{18}F]**9** when compared to the current reference standard for PDE10A-targeted PET, [^{18}F]MNI659. Further, dose—response experiments with a series of escalating doses of PDE10A inhibitor **1** in rhesus monkey brains confirmed the utility of [^{18}F]**9** for evaluating target occupancy *in vivo* in higher species. In conclusion, our results indicated that [^{18}F]**9** is a promising PDE10A PET radioligand for clinical translation.

1. Introduction

Cyclic adenosine monophosphate (cAMP) and guanosine monophosphate (cGMP) serve as critical intracellular second messengers that are involved in a myriad of downstream signaling pathways *via* activation of protein kinase A (PKA) and protein kinase G (PKG), respectively[1,2]. As such, cAMP and cGMP regulate a wide range of physiological processes including apoptosis, learning and memory, cell differentiation, ion channel function, insulin secretion, platelet aggregation, smooth muscle relaxation, and T-cell activation[3−6]. Cyclic nucleotide phosphodiesterase (PDE) enzymes, encoded by 21 human genes and categorized into 11 distinct families, provide the sole route for the downregulation of cAMP and/or cGMP, thereby regulating their intracellular levels. The latter is required for physiological functions of the central nervous system (CNS)[7−10]. In contrast to other members of PDE families, PDE10A was found to be expressed modestly in peripheral organs, with the exception of the testes, while abundant in the CNS, especially in the medium spiny neurons of the striatum[11−14]. Along this line, PDE10A plays pivotal roles in the regulation of signaling transduction from dopaminergic and glutamatergic input to the striatal medium spiny neurons[15]. The inhibition of PDE10A holds therapeutic potentials in neurologic and psychiatric disorders caused by dysfunction of the basal ganglia, of which the striatum constitutes a major component. As such, the development of PDE10A inhibitors has drawn continuous attention, with a number of preclinical and clinical studies recently reported[16−20]. Of note, the plant-derived PDE10A inhibitor, papaverine, was the first compounds that entered the clinical arena[21,22]. Nonetheless, the use of papaverine was hampered by the relatively low potency and selectivity, as well as the relatively fast *in vivo* clearance. Another PDE10A inhibitor with improved pharmacology, MP-10 (PF-2545920)[23,24], was tested for the treatment of PD and schizophrenia[25]. Despite promising preclinical findings, MP-10 treatment did not result in the anticipated antipsychotic effect in multiple clinical trial[24,25]. Underlying causes for the discrepancy between preclinical and clinical studies are likely of multifactorial origin and further studies are warranted. TAK-063 is another PDE10A inhibitor that

exhibited efficacy in animal models[26,27]. Although TAK-063 has proven to be safe in two phase I clinical trials, the primary endpoint of improving schizophrenia symptoms was not met in a clinical phase II study[26,27]. These results indicate that an improved understanding of species-differences is crucial to allow the successful translation of PDE10A inhibitors from rodent models to humans. PDE10A inhibitors that have been repurposed or are still under clinical development include, but are not limited to, TAK-063 and PBF-999[24].

Positron emission tomography (PET) imaging with highly specific radioligands[28] would enable noninvasive quantification of PDE10A, providing the opportunity to assess the function of PDE10A *in vivo* under physiological and pathophysiologic conditions[29,30]. Furthermore, dose—response experiments derived from PET would provide critical information on target occupancy of a candidate inhibitor at an administered dose[31,32], which would contribute to appropriate dosing with PDE10A inhibitors in early drug development, thereby ensuring sufficient exposure for efficacy and concurrently optimizing the risk-benefit profile of novel PDE10A inhibitors[33,34]. So far, several ^{11}C-labeled PDE10A radioligands were developed for imaging PDE10A in the living brain, such as [^{11}C]MP-10 ([^{11}C]**1**)[35], [^{11}C]IMA-107 ([^{11}C]**2**)[36−39], [^{11}C]Lu AE92686 ([^{11}C]**3**)[40,41] and [^{11}C]T-773[33] ([^{11}C]**4**) (Fig. 1A). However, the low *in vivo* specific binding and metabolic stability[36,42], as well as the relatively short half-life of ^{11}C hampered their broad application. On the other hand, ^{18}F exhibits several advantages of ^{11}C including better suitability for multistep radiolabeling procedures, multiple PET scans with a single production, radioligand storage and transportation due to more appropriate half-life (109.8 *vs.* 20.4 min), as well as smaller maximum positron energy (^{18}F *vs.* ^{11}C, 649 *vs.* 960 keV), which ultimately results in a higher spatial image resolution. As shown in Fig. 1B, the first reported ^{18}F labeled PDE10A radioligand was [^{18}F]JNJ-41510417 ([^{18}F]**5**, IC$_{50}$ = 0.5 nmol/L)[43]. The high ratio of plasma protein binding as well as slow kinetics *in vivo* prompted the research team at Johnson & Johnson to develop novel PDE10A candidates based on the same scaffold with reasonable lipophilicities and binding affinities[44,45]. Recently, the deuterated ^{18}F-analogs of **4** were developed to extend the

applications in clinical settings while maintaining the *in vivo* metabolic stability. Along this line, [^{18}F]FM-T-773-d_2 ([^{18}F]**6**, IC_{50} = 1.8 nmol/L) portrayed closely mimicking properties to [^{11}C]**4**, however, with improved stability, thus serving as an optimal tool for *in vivo* applications[46]. To date, [^{18}F]MNI659 ([^{18}F]**7**, IC_{50} = 0.097 nmol/L) constitutes the most sensitive, reliable and frequently used radioligand for clinical PDE10A imaging due to the favorable pharmacokinetics, specific binding and test-retest reliability[47−49]. However, the [^{18}F]fluoroethoxy motif in the structure of [^{18}F]**7** is prone to cytochrome-P450 monooxygenase metabolism, thereby complicating the neuroPET image analysis. Indeed, substitution of the [^{18}F]fluoroethoxy motif with a [^{18}F]fluoromethoxy-d_2 group proved to be beneficial for PET, as evidenced by the superior radiometabolic stability and higher BP_{ND} values of [^{18}F]**8** (K_i = 2.9 nmol/L) compared to the non-deuterated version, [^{18}F]**7** (Fig. 1)[50]. Nevertheless, since the purification of [^{18}F]fluoromethoxy-d_2 synthon (bp 15 °C) consisted of discreet distillation, series of Sep-Pak cartridges separation, followed by effective trapping in the hot cell[46,50], the automated synthesis of [^{18}F]**8** proved to be challenging in several radiochemistry facilities, thus impeding a broad clinical application.

We hypothesized that the direct attachment of ^{18}F to the inactive phenyl ring would maintain a reasonable binding affinity and lipophilicity of the ligand, as well as exhibit an improved *in vivo* metabolic profile due to the inherently inert features of aryl-^{18}F bonds. Therefore, the aims of this work were (i) to synthesize the novel PDE10A inhibitor **9** (P10A-1910), to determine its *in vitro* binding affinity, selectivity and physicochemical properties, (ii) to establish radiofluorination of **9** *via* the spirocyclic iodonium ylide (SCIDY) precursor and assess the brain penetration, metabolic stability and *in vitro/in vivo* specificity of [^{18}F]**9** towards PDE10A. Further, we envisioned, (iii) the assessment of its utility for *in vivo* target engagement studies in nonhuman primates.

2. Results and discussion

2.1. Chemical synthesis

To prepare PDE10A inhibitor **9** (P10A-1910) and the key radio-labeling precursor **15** containing the isoindoline-quinazolinone scaffold, we envisioned an efficient synthetic strategy that was based on previously reported synthetic procedures[51], however, with modifications. As shown in Scheme 1, starting with the commercially available 3-hydroxyphthalic anhydride **10**, nucleophilic substitution and intramolecular cyclization occurred under basic conditions, affording isoindoline-1,3-dione **11** in 33% yield.

Subsequent alkylation reaction installed the isopropyl group on the phenol moiety, followed by TFA-triggered esterolysis to afford the primary acid **13** in 68% yield over two steps. Reacting compound **13** with 2-amino-4-methylbenzoic acid and triphenyl phosphite in pyridine at 100 °C for 4 h, and subsequent treatment with 4-fluoroaniline yielded reference compound **9**. Similar condensation reactions were readily achieved in the presence of 4-iodoaniline, whereas carboxylic acid **13** was converted to aryl halide **14** in 47% yield over two steps. Oxone was used to oxidize **14** in a mixture of CHCl$_3$/TFA into the corresponding iodo(III) intermediate, which was then coupled with SPIAd under basic conditions to afford the SCIDY precursor **15** in high yield (72%, two steps from **14**).

2.2. Pharmacological and physiochemical properties

With target compound **9** in hand, the pharmacological and physicochemical properties were investigated. Fluorescence polarization (FP) was carried out to measure *in vitro* binding potency of **9** for PDE10A and its selectivity over other PDE subtypes. As shown in Table 1, the IC_{50} for PDE10A was 2.07 nmol/L, which was comparable to the lead structure **8** and is anticipated to provide sufficient binding potential for successful PDE10A-targeted PET imaging[50]. The binding affinities of **9** for other PDE subtypes including PDE1A/B/C, PDE2A, PDE3A/B, PDE4A/B/C/D, PDE5A, PDE7A, PDE8A, and PDE9A were tested (Supporting Information Fig. S1), and no significant inhibition was observed for concentrations up to 5 μmol/L, which demonstrated that **9** is highly selective for PDE10A. Log$D_{7.4}$ value of **9** was found to be 3.5 by the shake flask method, and the calculated topological polar surface area (tPSA) was 0.79 nm^2 (79 Å^2). Furthermore, MDCK-MDR1 experiment revealed an apparent permeability coefficient [$P_{app(A-B)}$] of 30 × 10^{-6} cm/s (values > 10 × 10^{-6} cm/s suggest high BBB permeability), indicating that the inhibitor **9** was able to penetrate the brain. Further, **9** was not a substrate of P-glycoprotein (P-gp), as evidenced by an MDR1 efflux ratio (ER) of 1.11. Overall, these
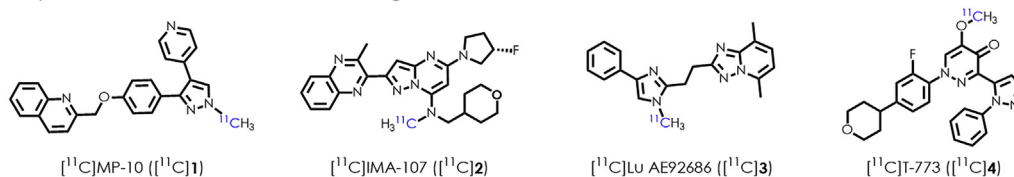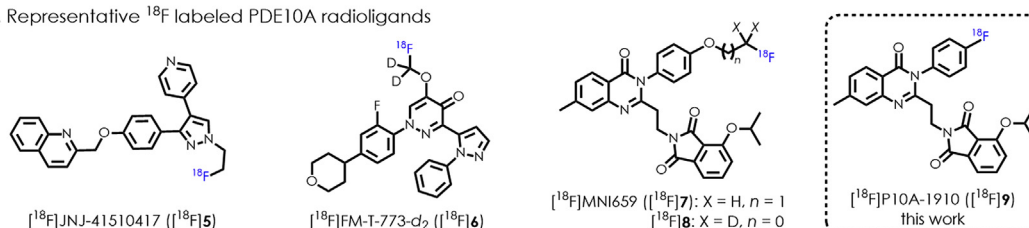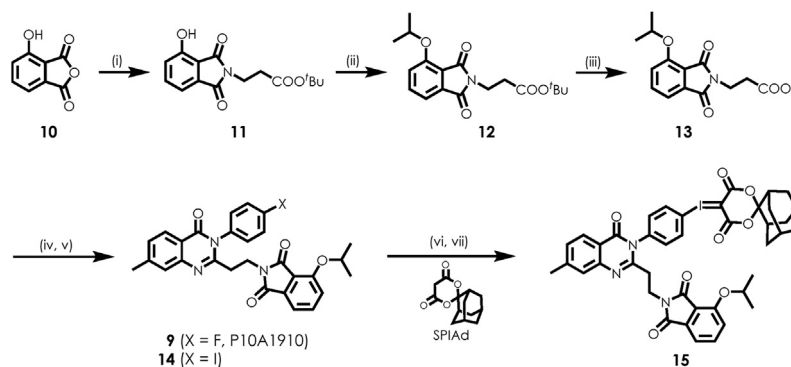

Figure 1   Representative radioligands for PET imaging of PDE10A.

Scheme 1   Syntheses of PDE10A inhibitor **9** and respective SCIDY precursor **15**. Reagents and conditions: (i) *tert*-butyl 3-aminopropanoate hydrochloride, NEt$_3$, 1,4-dioxane, 50 °C, overnight, 33% for **11**; (ii) *i*-PrI, Cs$_2$CO$_3$, CH$_3$CN, 80 °C, 4 h, 73% for **12**; (iii) TFA, DCM, room temperature, 4 h, 93% for **13**; (iv) triphenyl phosphite, 2-amino-4-methylbenzoic acid, pyridine 100 °C, 4 h; (v) 4-fluoroaniline, pyridine 100 °C, 4 h, 48% for **9** over two steps from **13**; or 4-iodoaniline, pyridine 100 °C, 4 h, 47% for **14** over two steps from **13**; (vi) oxone, TFA/CHCl$_3$, room temperature, 1 h; (vii) SPIAd, 10% Na$_2$CO$_3$ (aq), EtOH, room temperature, 1 h, 72% for **15** over two steps from **14**.

results strongly supported the radiolabeling of **9** and biological evaluation of [^{18}F]**9** as a PDE10A-targeted PET radioligand.

2.3. Radiochemistry

Encouraged by the promising pharmacology findings and based on our previous research on SCIDY-mediated radiofluorination[52−56], we envisioned to optimize the radiolabeling parameters, including bases, solvents, reaction temperature and labeling period to obtain the desired PET ligand [^{18}F]**9** with good labeling yield and molar activity. We initially conducted the radiolabeling in *N,N*-dimethylacetamide (DMAc) at 140 °C with several commonly used bases including KOAc/K$_{222}$ (1 mg/5 mg), K$_2$C$_2$O$_4$/K$_{222}$ (1 mg/5 mg), tetraethylammonium hydrogensulfate (TEAHS, 1 mg), tetrabutylammonium methanesulfonate (TBAOMs, 1 mg) and tetraethylammonium bicarbonate (TEAHCO$_3$, 1 mg). Our findings indicated that TEAHCO$_3$ provided the most favorable labeling efficiency with a radiochemical conversion (RCC) of approximately 20% (Fig. 2A). Further optimization showed a positive correlation between the RCC and reaction temperature in DMF, while the highest radiochemical conversion in DMAc (*ca.* 20%) was obtained at a reaction temperature of 140 °C (Fig. 2B). We next assessed the impact of reaction time and amount of TEAHCO$_3$ on RCC (Fig. 2C). The results showed that the amount of TEAHCO$_3$ was pivotal for the radiolabeling. Indeed, while 2 mg of TEAHCO$_3$ virtually suppressed the formation of [^{18}F]**9**, the use of low TEAHCO$_3$ amounts (0.5 mg) led to a significant improvement of

RCC (33% at 10 min). Notably, shortening of reaction time further improved the RCC (47% at 5 min). Interestingly, the only tested condition that led to a consistent increase of RCC over time was at 0.25 mg TEAHCO$_3$. Consequently, the low amount of base seemed to circumvent instability issues, however, at the cost of longer reaction times. At the end of the synthesis, [^{18}F]**9** was obtained in $25 \pm 5\%$ decay-corrected final yield (70 min total synthesis time) with >99% radiochemical purity and >111 GBq/μmol (3 Ci/μmol) molar activity. No radiolysis was detected by radio-HPLC up to 180 min after formulation with 5% DMSO, 5% Tween 80 and 90% sterile water. Further, [^{18}F]**9** was stable in mouse serum *in vitro* at 37 °C for 180 min.

2.4. *In vitro* autoradiography

To assess the binding specificity as well as the selectivity of [^{18}F]**9** towards PDE10A, we performed *in vitro* autoradiography (ARG) studies using wild-type Sprague−Dawley (SD) rat brain slices. Under baseline conditions (Fig. 3A), highest radioactivity was found to be accumulated in the striatum, while the cerebellum showed lowest radioactivity uptake, which was in accordance with the biological expression of PDE10A in the rodent brain[57,58]. Blocking experiments were conducted by incubating the brain slices with a mixture of [^{18}F]**9** (120 μCi/mL) and PDE10A high-affinity ligand **1** (10 μmol/L) and resulted in a dramatical reduction of striatal radioligand binding (Fig. 3B). Indeed, autoradiographic data quantification revealed a specificity of more than

Table 1   *In vitro* characterization of target compound **9**.

PDE10A IC$_{50}$ (nmol/L)	PDE selectivity	Log$D$ (pH 7.4)	tPSA (Å^2)	Permeability ($\times 10^{-6}$ cm/s)	P-gp (B−A/A−B)
2.07	>2500	3.5	79	30	1.1

[a]Concentration-response curve of **9** for the inhibition of PDE10A activity determined by human red blood cell (RBC) phosphodiesterase assay with TC-E 5005, a known PDE10A inhibitor, as a reference.
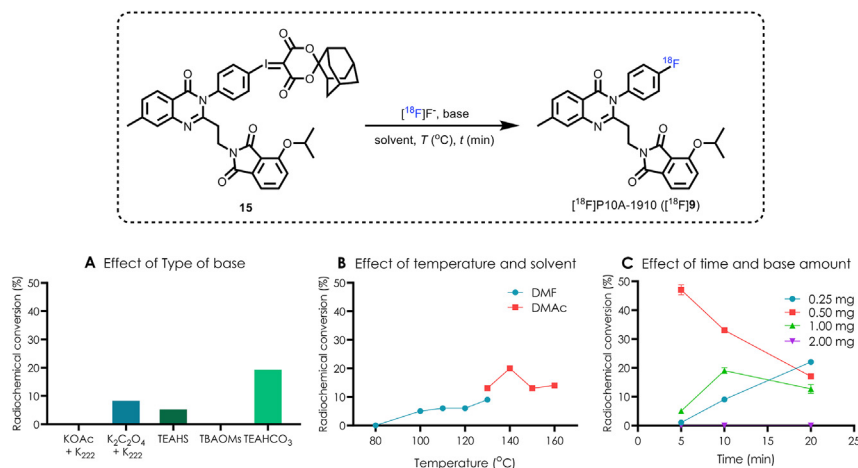
Figure 2 Optimization of [^{18}F]**9** radiosynthesis. [^{18}F]fluoride (111−185 MBq; 3−5 mCi) was added in each reaction. (A) Ylide (2 mg), DMAc (300 µL), base, 140 °C, 10 min. (B) Ylide (2 mg), DMF or DMAc (300 µL), TEAHCO$_3$ (1 mg), heated for 10 min. (C) Ylide (2 mg), DMAc (300 µL), TEAHCO$_3$ (indicated loadings), 140 °C. Radiochemical conversions were determined by radio-TLC, and the identity of ^{18}F-labeled radioligand was evaluated by radio-HPLC.

80%, as depicted in Fig. 3C. These results confirmed that [^{18}F]**9** possessed a high *in vitro* specificity towards PDE10A.

2.5. Whole-body biodistribution studies

The pharmacokinetic properties of [^{18}F]**9** were assessed using ICR mice, and the radioactivities in different tissues/organs were measured at a series of time points post injection. As shown in Fig. 4, the radioactivity in blood was rapidly cleared. High initial radioactivity uptake (%ID/g > 3) was found in the brain, lung, heart, kidney, liver, pancreas, and small intestine at 1 min pi. Subsequently, the radioactivity was washed out gradually in most organs, while gradually increased to the peak in liver and small intestine at 5 min post injection. The high uptake (%ID/g > 10) in the kidney, liver and small intestine indicated that [^{18}F]**9** may be excreted through both, the hepatobiliary and urinary system. Notably, radioactivity uptake in the bone remained low during all assessed time points, which indicated that [^{18}F]**9** did not undergo *in vivo* radiodefluorination.
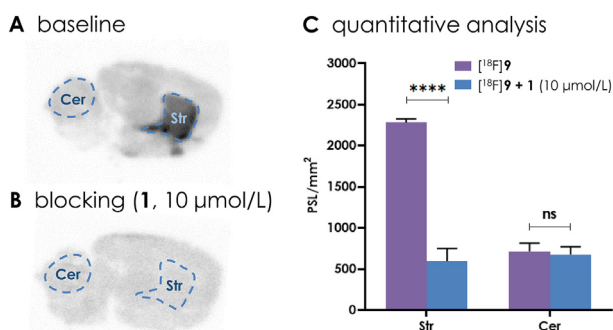

Figure 3 *In vitro* autoradiography of [^{18}F]**9** on rat brain sagittal sections. (A) Brain slices were incubated with [^{18}F]**9** (120 µCi/mL) for 30 min; (B) Brain slices were co-incubated with [^{18}F]**9** (120 µCi/mL) and **1** (10 µmol/L) for 30 min; (C) Quantitative analysis of [^{18}F]**9** specificity by comparison of baseline and blocking conditions. Str = striatum; Cer = cerebellum. Data are presented as mean ± SEM (*n* = 4) and analyzed by unpaired *t* test. Asterisks indicated statistical significance, ****$P \leq 0.0001$.

2.6. PET imaging studies in rat brains

To further corroborate the binding specificity of [^{18}F]**9** *in vivo*, dynamic microPET imaging (0−60 min) under different conditions were conducted in SD rats. Co-registration of averaged PET images (0−25 and 25−60 min) with MRI T1WI template, as well as the time−activity curves (TACs) of specific tissues are depicted in Fig. 5. The baseline study (Fig. 5A and D) demonstrated that [^{18}F]**9** rapidly entered the brain, whereby highest uptake levels were observed in the striatum (SUVmax = 1.4) within 1 min, followed by gradual washout. No obvious radioactivity accumulation was observed in other brain regions such as cerebral cortex, hippocampus and cerebellum. The neuro-distribution pattern of [^{18}F]**9** was found to be in agreement with previous reports of other PDE10A PET ligand[45,50].

To assess specific binding of [^{18}F]**9** to PDE10A, both pre-blocking and chase-blocking dynamic PET imaging studies were conducted with the injected dose as 5 mg/kg of PDE10A inhibitor **1**. As shown in Fig. 5B and E, pre-injection abolished the heterogenous distribution, leading to a significantly accelerated washout of radioactivity from the striatum (SUV$_{1\ min/60\ min}$ > 20). Administration of **1** at 25 min post injection of [^{18}F]**9** resulted in a substantially decreased PET signal in the striatum (75% *in vivo* specificity, Fig. 5C and F). The PET signal in the striatum was decreased to *ca.* 0.1 SUV at 60 min under both blocking conditions. These results demonstrated that [^{18}F]**9** exhibited a high *in vivo* specificity with a reversible binding mechanism.

2.7. Radiometabolite analysis

To investigate the metabolic stability of [^{18}F]**9** *in vivo*, we analyzed the radiometabolites in SD rats at two time points after tracer injection. Brain and plasma samples were harvested at 20 and 60 min pi, whereas the samples were analyzed by radio-HPLC and gamma counter[59]. As shown in Fig. 6, [^{18}F]**9** was relatively stable in the plasma with intact parent tracer fractions of 58% at 20 min and 43% at 60 min, respectively. Of note, we observed the formation of uncharacterized more polar radiometabolites in the plasma, however, these radiometabolites were not detected in the brain. Indeed, [^{18}F]**9** possessed excellent *in vivo* stability in the brain, with no detectable ^{18}F-labeled metabolites (unchanged fraction >96% at
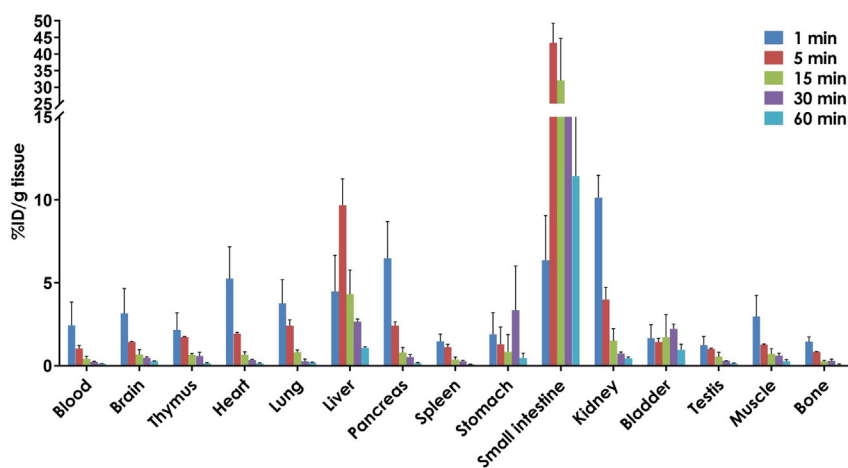
Figure 4 *Ex vivo* Biodistribution of [^{18}F]**9** in ICR mice. Data are expressed as injected dose per gram of wet tissue (%ID/g) with means ± standard deviations, $n = 3$.

both two time points). These results indicated that the radio-metabolites were not able to cross the BBB, rendering [^{18}F]**9** suitable for CNS-targeted imaging.

Although [^{18}F]MNI659 ([^{18}F]**7**) is currently considered the reference standard in PDE10A-targeted PET imaging, concerns have been raised with regard to its metabolic stability. Indeed, Zhang and co-workers[50] have recently shown the presence of brain radiometabolites following administration of [^{18}F]MNI659 to rodents[50]. Further, their research indicated that the replacement of the [^{18}F]fluoroethoxy moiety in the structure of [^{18}F]MNI659 by a deuterated [^{18}F]fluoromethoxy analog ultimately precluded the formation of brain radiometabolites, which points towards metabolic instability of the fluorine-18 bearing side chain of [^{18}F]MNI659. These results were further supported by the PET images

of Huntington's disease patients that were presented by Russel et al.[48], where skull uptake—an indicator of *in vivo* defluorination—seems evident, particularly in HD patients. While skull uptake can indeed complicate brain image analysis *via* partial volume effects as well as differences in enzymatic activity across individuals (for instance, between patient and healthy subject), *in vivo* defluorination is more likely to occur in aliphatic than in aromatic radiofluorines[60]. Notwithstanding the lack of clinical data with [^{18}F]**9**, preclinical findings indicate an improved metabolic profile of [^{18}F]**9**, as compared to [^{18}F]MNI659, which is evidenced by the lack of brain radiometabolites and the higher fraction of intact parent tracer in the plasma at 20 and 60 min post injection in rats[50]. Of note, we did not observe any defluorination by *in vitro* assays with human liver microsomes (Supporting
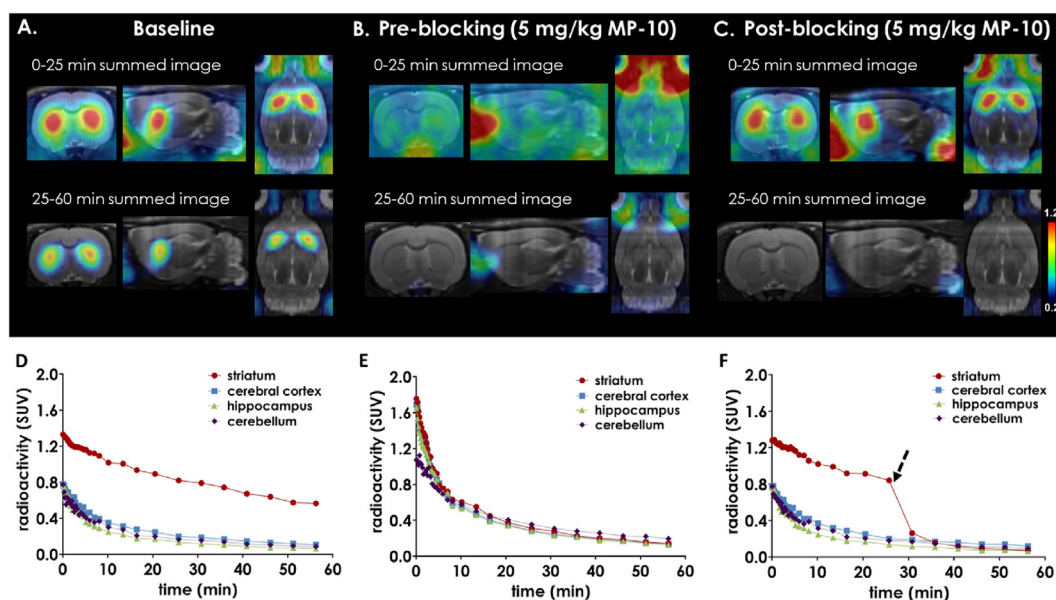
Figure 5 PET studies of [^{18}F]**9** in the rat brain. (A)–(D) Representative PET-MRI images and TACs in various brain regions of interest under baseline conditions; (B)–(E) representative PET-MRI images and TACs in various brain regions of interest under blocking conditions (pre-injection of MP-10, iv); (C)–(F) representative PET-MRI images and TACs in various brain regions of interest under blocking conditions (post-injection of MP-10, iv).
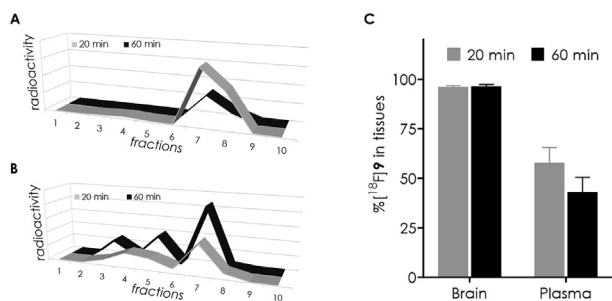
Figure 6 *Ex vivo* radiometabolite analysis of [¹⁸F]**9** in the brain and plasma of rats at 20 and 60 min post-injection. (A) Representative reconstructive radiochromatograms of the rat brain samples; (B) Representative reconstructive radiochromatograms of the rat plasma samples showing two detectable polar radiometabolite fractions; (C) Quantitative analysis of intact [¹⁸F]**9** fraction. Data are presented as mean ± SD ($n = 3$).

Information Fig. S3). Future clinical studies will unveil whether this improved stability will translate into enhanced performance characteristics in patients.

2.8. Dose-response studies in the rhesus monkey brain

Given that neuroPET imaging on higher species, such as non-human primate (NHP), typically provides crucial insights for clinical translation, and encouraged by the promising results obtained from experiments in rodent, our efforts then focused on PET imaging studies in rhesus monkey to explore brain penetration, regional distribution and clearance of [¹⁸F]**9**. Representative averaged PET images (20−60 min) in rhesus brain and corresponding TACs under baseline and blocking conditions (pretreatment with indicated dose of **1**) are shown in Fig. 7. [¹⁸F]**9** was brain penetrant, whereas the radioactivity was specifically accumulated in striatum with highest standardized uptake values (SUVs) > 3.0. Importantly, a dose-dependent PET signal
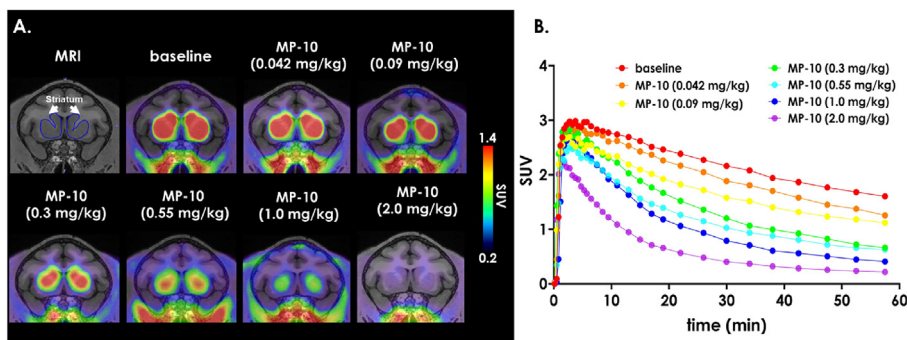
Figure 7 PET studies of [¹⁸F]**9** in the rhesus monkey brain. (A) Representative summed PET images (20−60 min) under baseline and dose-dependent blocking conditions (pre-injection of MP-10, iv); (B) TACs representing striatal radioligand accumulation under baseline and dose-dependent blocking conditions.
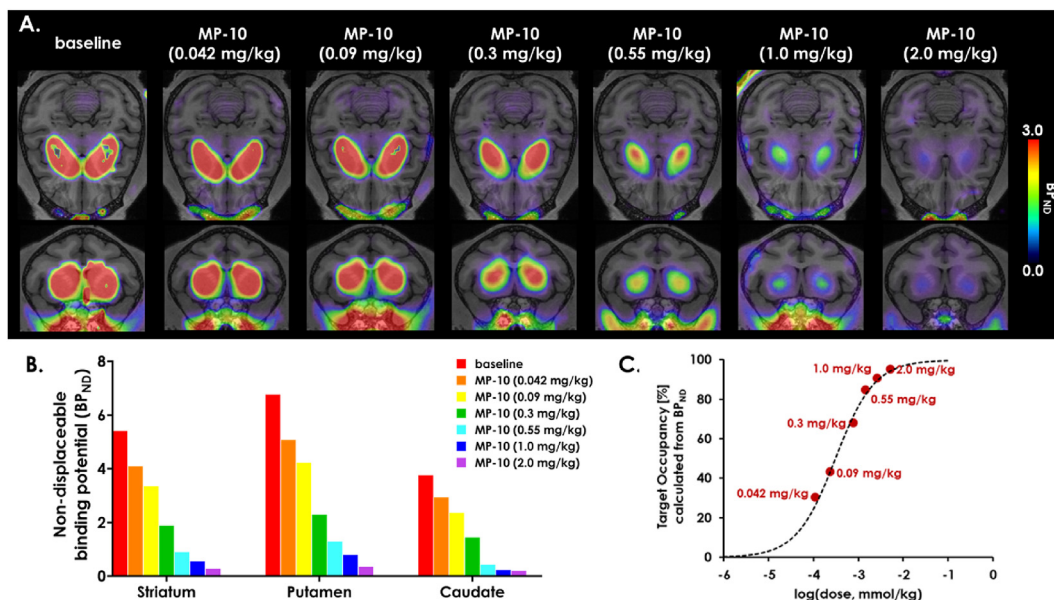
Figure 8 Kinetic modeling analysis and target occupancy assessment. (A) Representative PET images presented as non-displaceable binding potential (BP_ND) under baseline and blocking conditions; (B) BP_ND in striatum, putamen and caudate under baseline and blocking conditions; (C) target occupancy of PDE10A inhibitor MP-10 using [¹⁸F]**9** in the rhesus monkey striatum, calculated from BP_ND. An ID_50 (iv dose at which 50% target occupancy was achieved) value of 0.3 µmol/kg was estimated.

reduction was achieved with escalating doses of **1**, a PDE10A inhibitor with documented clinical efficacy[34,61], thus underscoring the utility of [^{18}F]**9** for target engagement studies in higher species.

Given the reported lack of PDE10A expression in the cerebellum[12], we performed kinetic modeling applying the simplified reference tissue model (SRTM)[62] with the cerebellum as pseudo-reference region[63,64]. To assess the validity of the SRTM model for [^{18}F]**9**, we analyzed the time−activity curves in the cerebellum under baseline conditions ([^{18}F]**9** only), as well as following low dose and high dose MP-10 treatment. Notably, we did not observe any differences in the time−activity curves under baseline and blocking conditions, indicating that there was no specific binding of [^{18}F]**9** in the cerebellum (Supporting Information Fig. S5). Parametric brain images derived from non-displaceable binding potentials (BP$_{ND}$) are depicted in Fig. 8A. With escalating doses of **1**, the BP$_{ND}$ gradually decreased from 24% to 95%, as compared to baseline condition. Indeed, the decrease of BP$_{ND}$ was particularly observed in putamen and caudate (Fig. 8B). *In vivo* estimation of target occupancy by PET is critical to determine the dose at which a drug candidate occupies sufficient biological target to elicit therapeutic efficacy in patients. Therefore, a series of BP$_{ND}$ derived from the dose−response study were applied to determine *in vivo* target occupancy of **1**. As shown in Fig. 8C, the relationship between inhibitor dosing and target occupancy displayed a good fit by four parameters logistic nonlinear regression[65]. The dose of inhibitor **1** required to achieve 50% target occupancy (ID$_{50}$) was calculated to be 0.3 μmol/kg. In all, this study not only presented that the parametric brain mapping with BP$_{ND}$ was suitable to visualize the dose−response effects with high sensitivity, but also demonstrated the utility of [^{18}F]**9** in facilitating optimal dose finding for PDE10A-targeted drug candidates.

3. Conclusions

We have designed and synthesized a novel PDE10A inhibitor **9** with good binding affinity and selectivity. The corresponding ^{18}F-isotopologue, [^{18}F]**9** (designated [^{18}F]P10A-1910), was successfully radiolabeled in high radiochemical yields and purities *via* the SCIDY methodology. *In vitro* autoradiography on brain slides, *ex vivo* whole-body biodistribution, neuroPET imaging and *in vivo* metabolic studies in rats showed that [^{18}F]**9** exhibited sufficient brain penetration, reversible and specific binding, and good stability, which was superior to the clinically used reference standard for PDE10A-targeted PET imaging, [^{18}F]MNI659. Subsequent dose−response studies in NHPs demonstrated the utility of [^{18}F]**9** for assessing target engagement of PDE10A inhibitors. Our findings indicate that [^{18}F]**9** harbors enormous potential for successful clinical translation, thereby facilitating PDE10A-targeted drug discovery and contributing to a better understanding of PDE10A-related CNS pathologies.

4. Experimental

4.1. General information

All commercial reagents were purchased from Sigma−Aldrich, and used as received. Unless otherwise noted, solvents were freshly dried and degassed according to the purification handbook Purification of Laboratory Chemicals before using. Analytical

thin-layer chromatography (TLC) was performed on pre-coated glass-backed plates (EMD TLC silica gel 60 F254) and visualized using a UV lamp (254 nm) or potassium permanganate. Silica gel for flash chromatography was 300−400 mesh. ^{1}H, ^{13}C, and ^{19}F NMR spectra were recorded on Bruker 300, 400, 500 MHz on Bruker spectrometers, and resonances chemical shifts (δ) were given in parts per million (ppm) relative residual solvent (^{19}F chemical shifts are unreferenced unless otherwise noted). Peak multiplicities are abbreviated by the following symbols: s, singlet, brs, broad singlet; d, doublet; t, triplet; q, quartet; hept, heptahedron; m, multiplet; dd = doublet of doublets. HRMS spectra were measured on a Thermo Scientific LTQ Qrbitrap XL using ESI$^+$.

The rodent animal protocols were accredited by the Animal Ethics Committee at Jinan University, and the rhesus imaging studies were conducted following the ethical rules of Animal Care and Use Committee of Guangdong Landau Biotechnology Co. Ltd., which were approved by Association for Assessment and Accreditation of Laboratory Animal Care (AAALAC).

4.2. Chemical synthesis

tert-Butyl 3-(4-hydroxy-1,3-dioxoisoindolin-2-yl)propanoate (**11**). To a solution of 3-hydroxyphthalic anhydride (4.9 g, 30 mmol) and NEt$_3$ (90 mmol) in 1,4-dioxane (60 mL) was added *tert*-butyl 3-aminopropanoate hydrochloride (33 mmol). After stirring at 50 °C overnight, the reaction was quenched with water, then extracted with ethyl acetate. The organic layers were washed with brine, dried over Na$_2$SO$_4$ and concentrated under reduced pressure. Compound **11** was prepared as a white solid (33%) and used directly for next step without further purification.

tert-Butyl 3-(4-isopropoxy-1,3-dioxoisoindolin-2-yl)propanoate (**12**, reported compound[51]). To a mixture of **11** (2.9 g, 10 mmol), 2-iodopropane (20 mmol) and Cs$_2$CO$_3$ (35 mmol) was added CH$_3$CN (50 mL), and then stirred at 80 °C for 4 h. After cooling to ambient temperature, the mixture was filtered and concentrated under reduced pressure. The crude compounds were purified by chromatography on silica gel (Hexane:EtOAc = 5:1), and compound **12** was prepared as a white solid (73%). ^{1}H NMR (400 MHz, CDCl$_3$) δ: 7.60 (dd, J = 8.4, 7.3 Hz, 1H), 7.40 (d, J = 6.9 Hz, 1H), 7.17 (d, J = 8.4 Hz, 1H), 4.76 (hept, J = 6.1 Hz, 1H), 3.92−3.87 (m, 2H), 2.62 (t, J = 7.4 Hz, 2H), 1.44 (s, 3H), 1.43 (s, 3H), 1.40 (s, 9H).

3-(4-Isopropoxy-1,3-dioxoisoindolin-2-yl)propanoic acid (**13**, reported compound[51]). To a solution of intermediate **12** (1.7 g, 5 mmol) in dichloromethane (5 mL) was added dropwise trifluoroacetic acid (5 mL) at ambient temperature. After stirring for 4 h, the solvent was removed under reduced pressure. Compound **13** was prepared as a white solid (93%) and used directly for next step without further purification. ^{1}H NMR (400 MHz, CDCl$_3$) δ: 8.50 (brs, 1H), 7.61 (dd, J = 8.4, 7.3 Hz, 1H), 7.40 (d, J = 7.2 Hz, 1H), 7.18 (d, J = 8.5 Hz, 1H), 4.76 (hept, J = 6.1 Hz, 1H), 3.95 (t, J = 7.4 Hz, 2H), 2.77 (t, J = 7.4 Hz, 2H), 1.44 (s, 3H), 1.43 (s, 3H).

2-(2-(3-(4-Fluorophenyl)-7-methyl-4-oxo-3,4-dihydroquinazolin-2-yl)ethyl)-4-isopropoxyisoindoline-1,3-dione (P10A-1910, **9**). To a solution of intermediate **13** (500 mg, 0.8 mmol), 2-amino-4-methylbenzoic acid (0.8 mmol) and triphenyl phosphite (1.2 mmol) in pyridine (10 mL) was stirred under argon atmosphere at 100 °C for 4 h. After 4-fluoroaniline (0.88 mmol) added under argon atmosphere, the mixture was stirred for another 4 h. After cooling to ambient temperature, the solvent was removed under reduced pressure. The crude compounds were purified by chromatography on silica gel (hexane:EtOAc = 2:1), and PDE10A inhibitor **9** was prepared as a

white solid in 48% yield. ^{1}H NMR (500 MHz, CDCl$_3$) δ: 8.10 (d, $J = 8.1$ Hz, 1H), 7.57 (dd, $J = 8.5$, 7.2 Hz, 1H), 7.34 (d, $J = 7.2$ Hz, 1H), 7.32 (s, 1H), 7.30−7.24 (m, 3H), 7.20 (t, $J = 8.5$ Hz, 2H), 7.14 (d, $J = 8.4$ Hz, 1H), 4.68 (p, $J = 6.1$ Hz, 1H), 4.06 (t, $J = 7.4$ Hz, 2H), 2.69 (t, $J = 7.4$ Hz, 2H), 2.45 (s, 3H), 1.38 (s, 3H), 1.37 (s, 3H). ^{13}C NMR (125 MHz, CDCl$_3$) δ: 168.0, 166.8, 162.9 (d, $J = 249.8$ Hz), 162.4, 155.6, 153.3, 147.3, 145.6, 135.8, 134.6, 132.9 (d, $J = 0.1$ Hz), 130.4 (d, $J = 8.5$ Hz), 128.5, 127.1, 126.9, 120.6, 118.5, 118.3, 117.2 (d, $J = 23.0$ Hz), 115.5, 72.6, 34.9, 33.7, 22.0. ^{19}F NMR (470 MHz, CDCl$_3$) δ: −111.39−111.51 (m). HRMS (m/z, ESI) calcd for C$_{28}$H$_{24}$FN$_3$O$_4$Na$^+$ 508.1649, found 508.1644.

2-(2-(3-(4-Iodophenyl)-7-methyl-4-oxo-3,4-dihydroquinolin-2-yl)ethyl)-4-isopropoxyisoindoline-1,3-dione (**14**). The key iodo compound **14** was prepared in a similar manner as described for **9**. The crude compounds were purified by chromatography on silica gel (hexane:EtOAc = 2:1), and compound **14** was prepared in 47% yield as a light yellow solid. ^{1}H NMR (400 MHz, CDCl$_3$) δ: 8.14 (d, $J = 8.1$ Hz, 1H), 7.89−7.85 (m, 2H), 7.61 (dd, $J = 8.5$, 7.2 Hz, 1H), 7.41−7.35 (m, 2H), 7.30 (d, $J = 1.6$ Hz, 1H), 7.18 (d, $J = 8.4$ Hz, 1H), 7.11−7.05 (m, 2H), 4.72 (hept, $J = 6.0$ Hz, 1H), 4.12−4.06 (m, 2H), 2.75−2.68 (m, 2H), 2.49 (s, 3H), 1.42 (s, 3H), 1.41 (s, 3H). ^{13}C NMR (100 MHz, CDCl$_3$) δ: 167.9, 166.7, 165.6, 162.0, 155.5, 152.8, 149.8, 147.2, 145.6, 139.3, 136.7, 135.7, 134.5, 130.4, 128.5, 127.0, 126.8, 120.6, 118.3, 115.4, 95.2, 72.5, 34.7, 33.6, 21.93, 21.91. HRMS (m/z, ESI) calcd for C$_{28}$H$_{24}$IN$_3$O$_4$Na$^+$ 616.0709, found 616.0704.

2-(2-(3-(4-(((2′S,3a′S,5′R)-4,6-Dioxooctahydrospiro[[1,3]dioxane-2,7′-[2,5]methanoinden]-5-ylidene)-l3-iodaneyl)phenyl)-7-methyl-4-oxo-3,4-dihydroquinolin-2-yl)ethyl)-4-isopropoxyisoindoline-1,3-dione (**15**). To a solution of intermediate **14** (120 mg, 0.2 mmol) in CHCl$_3$ (0.3 mL) was added dropwise trifluoroacetic acid (1.0 mL) at room temperature. Then oxone (184 mg, 0.3 mmol) was added, and the mixture was stirred for 1 h. After concentrating the residue under reduced pressure, the residue was mixed with EtOH (5 mL) and added dropwise SPIAd (95 mg, 0.4 mmol) dissolved in 10% Na$_2$CO$_3$ aqueous solution (0.5 mL). After stirring at room temperature for 1 h, the reaction was quenched with water and extracted with dichloromethane for three times. Then, the organic layers were washed with brine and dried with MgSO$_4$. After concentrated under reduced pressure, the crude compounds were purified by chromatography on silica gel (hexane:EtOAc = 1:1) to obtain the SCIDY precursor **15** as a white solid (72%). ^{1}H NMR (400 MHz, DMSO-d_6) δ: 7.95 (dd, $J = 11.7$, 8.5 Hz, 3H), 7.70 (t, $J = 7.8$ Hz, 1H), 7.61 (d, $J = 8.3$ Hz, 2H), 7.43 (d, $J = 8.4$ Hz, 1H), 7.33 (dd, $J = 11.1$, 7.5 Hz, 3H), 4.79 (p, $J = 6.1$ Hz, 1H), 3.88 (t, $J = 7.1$ Hz, 2H), 2.63 (t, $J = 6.8$ Hz, 2H), 2.43 (s, 3H), 2.35 (s, 2H), 1.94 (d, $J = 11.9$ Hz, 4H), 1.77 (s, 2H), 1.72−1.57 (m, 6H), 1.28 (s, 3H), 1.27 (s, 3H). ^{13}C NMR (100 MHz, DMSO-d_6) δ: 167.9, 166.5, 163.1, 161.5, 155.2, 153.9, 147.3, 145.7, 139.6, 139.0, 136.7, 134.4, 133.6, 131.9, 128.7, 126.9, 126.6, 121.3, 118.4, 117.8, 116.7, 115.3, 105.7, 71.9, 57.8, 38.9, 37.0, 35.3, 34.79, 34.78, 33.6, 33.5, 33.4, 26.4, 22.1, 21.8. HRMS (m/z, ESI) calcd for C$_{41}$H$_{38}$IN$_3$O$_8$Na$^+$ 850.1601, found 850.1599.

4.3. Pharmacological and physicochemical properties

4.3.1. Potency and selectivity assays for P10A-1910 (**9**)
Compound **9** was dissolved in DMSO and stored at −20 °C. To assess the binding affinity towards PDE10A, **9** was tested in a 10-dose IC$_{50}$ study with 3-fold serial dilution starting at 1 μmol/L, while the control compound, TC-E 5005[66], was tested in a 10-dose

IC$_{50}$ with 3-fold serial dilution starting at 10 μmol/L ($n = 3$). To assess binding selectivity, **9** was tested in a single dose duplicate at a concentration of 5 μmol/L, and control compounds (IBMX for PDE1A/B/C, PDE2A, PDE3A/B, PDE4A/B/C/D; methoxyquinazoline for PDE5A; BRL-50481 for PDE7A; TC-E 5005 for PDE8A; zaprinast for PDE9A) were tested in a 10-dose IC$_{50}$ with 3-fold serial dilution starting at different concentrations. PDE1A/B/C, PDE2A, PDE3A/B, PDE4A/B/C/D, PDE5A, PDE7A, PDE8A, PDE9A, were diluted in reaction buffer 10 mmol/L Tris, pH 7.5, 5 mmol/mL MgCl$_2$, 0.01% Brij 35, 1 mmol/L DTT and 1% DMSO, respectively, while PDE1A, PDE1B and PDE1C were dissolved in the reaction buffer plus 0.2 mmol/L CaCl$_2$ and 0.36 μmol/mL CaM. Test compounds were added using Acoustic Technology (Echo550; nanoliter range). Different substrate concentrations were added for different assays (1 μmol/L cAMP for PDE3A, PDE3B, PDE4A, PDE4B, PDE4C, PDE4D, and PDE8A; 0.2 μmol/L cAMP for PDE7A; 1 μmol/mL cGMP for PDE1A, PDE1B, PDE1C, PDE2A and PDE5A; 0.2 μmol/L cGMP for PDE9A) and incubated for 1 h at room temperature. Fluorescence polarization (FP)[67] was measured after incubation at room temperature. For PDE3A, PDE3B, PDE4A, PDE4B, PDE4C, PDE4D, PDE7A, and PDE8A, standard curves were generated using nonlinear regression with a variable slope by GraphPad Prism using AMP as the reaction product, while for PDE1A, PDE1B, PDE1C, PDE2A, PDE5A and PDE9A, GMP was determined as the product.

4.3.2. Measurement of lipophilicity
To measure the lipophilicity, [^{18}F]P10A-1910 was first added into a mixture of n-octanol and PBS aqueous solution (0.1 mol/L) that both were pre-saturated with each other before use. After vortexing for 5 min, n-octanol and PBS were separated into sample tubes ($n = 3$) and centrifuged for 5 min (3500−4000 rpm) to ensure proper phase separation. Subsequently, the weight and radioactivity (using PerkinElmer 2480 Wizard automatic gamma counter) were measured and the log$D$ was calculated based on the radioactivity distribution between organic and aqueous layer.

4.3.3. Measurement of permeability
Madin−Darby Canine Kindy-Multidrug Resistance Protein 1 (MDCK-MDR1) model was used to investigate the permeability of **9** according to the literature[68], with the concentration of 1 μmol/L. The transport studies were used on inserts consisting of two interseptal structures (apical and basolateral), separated by MDCK-MDR1 cell monolayers. *Trans*-epithelial electrical resistance (TEER) value was measured to monitor the integrity of the MDCK-MDR1 cell monolayers. The assays were carried out in hank's balanced salt solution (HBSS) buffer along with 5 μmol/L Lucifer Yellow (LY) and 0.4% DMSO (pH 7.4). Eqs. (1)−(5) were used as follows:

$$\text{TEER} = (\text{Resistance sample}-\text{Resistance blank}) \times \text{Effective membrane area} \tag{1}$$

where TEER value of MDCK-MDR1 monolayers from random wells was 445 ± 22 Ω·cm^2 (mean ± SD, cell monolayer will be used if TEER value > 100 Ω·cm^2).

$$P_{\text{app}} = [V_A/(\text{Area} \times \text{Time})] \times (\text{Candidate}_{\text{accepter, 90-min}} /[(\text{Candidate}_{\text{donor, 0-min}}) \times \text{Dilution factor}] \tag{2}$$

$$P_{app(LY)} = [V_A/(Area \times Time)] \times (RFU_{accepter,\ 90\text{-}min} - RFU_{blank})/$$
$$(RFU_{donor,\ 0\text{-}min} - RFU_{blank}) \qquad (3)$$

$$Mass\ recovery\ (\%) = 100 \times (V_D \times Candidate_{donor,\ 90\text{-}min}$$
$$\times Dilution\ factor + V_A$$
$$\times Candidate_{acceptor,\ 90\text{-}min}) /$$
$$(V_D \times Candidate_{donor,\ 0\text{-}min}$$
$$\times Dilution\ factor) \qquad (4)$$

$$Efflux\ ratio = P_{app(B-A)}/P_{app(A-B)} \qquad (5)$$

were then calculated to assess the activity of transporters on drug kinetics across the model.

4.4. Radiolabeling of [^{18}F]P10A-1910

[^{18}F]F$^-$ was generated *via* the ^{18}O(p,n)^{18}F reaction that occurred in a 10 MeV cyclotron (GE, Qilin) with the protons bombarded on >98% enriched H$_2$^{18}O (TAIYO NIPPON SANSO Corporation, Tokyo, Japan). After pretreatment with 10 mL of 7.5% aqueous NaHCO$_3$ and washing with 20 mL of H$_2$O, the Sep-Pak QMA cartridge was used to trap the radioactivity [^{18}F]fluoride (1.48−1.85 GBq; 40−50 mCi) from the female side, and the solvent on the cartridge was removed with 20 mL of air. The elution of [^{18}F]fluoride was achieved with a solution of TEAHCO$_3$ (0.5 mg) in MeOH (1.0 mL) from the male side of the QMA into a 4 mL vial, and the mixture was then dried at 110 °C under a flow of nitrogen gas for 10 min. A solution of precursor **15** (2.0 mg) in anhydrous DMAc (300 μL) was then transferred into the vial, and the vial was heated at 140 °C for 5 min under nitrogen atmosphere. After cooling down by ice water, 600 μL of CH$_3$CN/H$_2$O (v/v, 1/2) was added to quench and dilute the mixture, then loaded into a semipreparative radio-HPLC system. A semipreparative column (Phenomenex Luna C18, 250 mm × 10 mm, 5 μm) was used with CH$_3$CN/H$_2$O (v/v, 1/1) as the elution at a flow rate of 5 mL/min. Retention time (t_R) for [^{18}F]P10A-1910 ([^{18}F]**9**) was 21 min. The radiolabeled product [^{18}F]**9** was collected and diluted with 100 mL of sterile H$_2$O, and then trapped on a Waters C18 Light cartridge that was pre-activated with 5 mL of ethanol and washed with 10 mL of sterile H$_2$O. [^{18}F]**9** was recovered with 1.5 mL of CH$_3$CN and then concentrated at 80 °C under a flow of N$_2$ for 10 min. The concentrated product then was reformulated in a mixture of 5% DMSO, 5% Tween 80, and 90% sterile water. An analytical HPLC system equipped with a XSelect™ HSS TS column (4.6 mm × 150 μm, 5 μm) was used to analyze the radiochemical and chemical purity, as well as the molar activity of the product, with the mobile phase of CH$_3$CN/H$_2$O (v/v, 1/1) at flow rate of 1 mL/min (t_R: 15 min). UV detector was set at 254 nm. The identity of [^{18}F]**9** was confirmed by co-injection of reference target compound **9** (P10A-1910).

4.5. In vitro autoradiography studies in rat brain slices

Sagittal brain slices (20 μm sections, stored at −80 °C) were preincubated with 218 mL of Tris-HCl buffer (50 mmol/L, pH 7.4) consisting of MgCl$_2$ (2 mmol/L) and CaCl$_2$ (1.2 mmol/L) in a glass reservoir for 20 min containing at room temperature. For baseline conditions, slices were incubated in the above buffer containing [^{18}F]**9** (120 μCi in 2 mL of buffer) for 30 min. In terms of blocking studies, the well-described PDE10A inhibitor PF-2545920 (**1**, also codenamed MP-10, 2 mL) was used with the

concentration of 10 μmol/L. After incubation, all brain sections (4 slices for each condition) were immersed with cold fresh buffer for three times (3 min for each one), followed by cold sterile water once (3 min), and then dried by cold air. The brain slices were exposed for 45 min to the imaging plates (Amersham Typhoon, Cytiva, USA). Autoradiograms were generated and photo-stimulated luminescence (PSL)/tissue area (mm^2) values in striatum and cerebellum were performed using a Bio-Imaging Analyzer System (Multi Gauge Version 2.3, FUJIFILM).

4.6. Biodistribution studies in mice

ICR mice (male, 8 weeks, 25−30 g) were maintained on a 12 h light/12 h dark cycle and provided water ad libitum. 50 μCi (1.85 MBq) of [^{18}F]**9** (100 μL) was intravenously injected to each mouse *via* the tail vein. At the indicated time point, mice (n = 3) were sacrificed by dislocation of cervix, and organs such as whole brain, thymus, heart, liver, lungs, spleen, pancreas, stomach, small intestine, kidneys, bladder, testis, muscle, bone and blood samples were immediately collected and weighted. A 2480 Wizard automatic gamma counter (PerkinElmer, USA) was used for determining each organ's radioactivities, which were decay-corrected back to the [^{18}F]**9** injection time point according to the half-life of ^{18}F.

4.7. In vivo small-animal PET imaging studies with rat brains

Dynamic PET imaging was carried out using a PET/CT scanner (Bruker, MA, USA). During the scan, the mixed gas (2% (v/v) isoflurane in oxygen) were used for anesthesia. 0.6−0.8 mCi (22.2−29.6 MBq) of [^{18}F]**9** (250 μL) was intravenously administrated into the rat *via* a preinstalled 24-gauge catheter, and rat brain dynamic PET scans were acquired for 60 min in a 3D list mode. For blocking conditions, MP-10 **1** (5 mg/kg) was administrated before injection of [^{18}F]**9**, or at 25 min post tracer injection. PMOD software (version 4.006) was used to generate the representative PET images (co-registered with the rat brain MRI template) and analyze the TACs from VOI in the cerebral cortex, striatum, hippocampus and cerebellum. The radioactivity was characterized by SUV.

4.8. Radiometabolite analysis

Under isoflurane anesthesia, SD rats (n = 3, each time point) were decapitated at 20 and 60 min post injection of [^{18}F]**9**. The blood and whole brain were then harvested immediately. The rat brain was cooled on ice, homogenized in 50% CH$_3$CN in H$_2$O on ice, and then centrifuged for 2.5 min at 4 °C (14,500×g). The supernatant was recovered. Similarly, the supernatant (0.5 mL) of blood samples was collected and mixed with ice-cooled CH$_3$CN (0.5 mL). The residue was vortexed for 20 s and again centrifuged for 2.5 min at 4 °C (14,500×g) for deproteinization. Both, brain and plasma homogenates were mixed with an aliquot of standard compound **9** (P10A-1910, 20 μL), and co-injected into the radio-HPLC system with a UV detector set on 264 nm. The samples were separated into ten sections (1 min for each section) using an analytical column (Phenomenex Luna C18, 250 mm × 10 mm, 5 μm), and with 70% CH$_3$CN in water as mobile phase for elution (5.0 mL/min). The radioactivity for each section was measured by a 2480 Wizard automatic gamma counter (PerkinElmer, USA), and the counts were all decay-corrected. The radiochromatograms were reconstructed, and the

percentage of [^{18}F]**9** (standard UV peak as an indicator on HPLC) to total radioactivity was measured as [(counts for sections 6−9)/(total counts)] × 100.

4.9. PET-MRI imaging studies on rhesus monkey

T1-weighted MR anatomical images were acquired on a 3.0 T scanner. A rhesus monkey was anesthetized by intramuscular injection of ketamine (10 mg/kg), and then put on the scanning bed in the supine position. The whole-brain images were acquired with a 3D Bravo T1 sequence.

The rhesus monkey used for PET/CT scan was allowed only water for 14−16 h before the radioligand injection, but allowed to drink water at any time. A male rhesus (weight range 6.01−6.85 kg) underwent PET scan. The subject was initially anesthetized with ketamine (10 mg/kg; im), put on the scanning bed, and maintained in light narcosis with 2% isoflurane and 98% oxygen. The rhesus was supine, and a stereotactic frame was used to fix the position of head. A solution of [^{18}F]**9** (3.57−4.12 mCi) was injected into the monkey through an intravenous indwelling needle, followed by a dynamic PET scan of the head for 60 min. For the blocking studies, MP-10 **1** (in the order of 0.042, 0.09, 0.3, 0.55, 1.0, 2.0 mg/kg) was injected intravenously, followed by the injection of [^{18}F]**9**. Each PET/CT scan was conducted with an interval of no less than two weeks.

The PET and MR images were co-registered according to the method of literature[69]. The co-registered PET images were converted to brain template MR and single MR image using the same parameters[70]. TACs, derived from the VOIs, were presented as SUV which were decay-corrected back to the radioligand injection time point.

Acknowledgments

Author contributions

All the authors contributed to this manuscript and have approved its final version. Steven H. Liang and Lu Wang proposed the study and conceived project. Zhiwei Xiao, Huiyi Wei and Lu Wang wrote the manuscript. Steven H. Liang and Ahmed Haider modified the paper. Zhiwei Xiao, Huiyi Wei, Yi Xu, Junjie Wei, Shiyu Yuan, Jian Rong, Chunyu Zhao, Guocong Li, Weibin Zhang, Huangcan Chen, Yuefeng Li, Lingling Zhang, Jiyun Sun, Shaojuan Zhang, Qijun Cai and Lu Hou performed experiments. Hai-Bin Luo, Sen Yan, and Chao Che designed and guided experiments.

Conflicts of interest

The authors declare no conflicts of interest.

Appendix A.   Supporting information

Supporting information to this article can be found online at https://doi.org/10.1016/j.apsb.2021.11.014.

References

1. Beavo JA, Brunton LL. Cyclic nucleotide research—still expanding after half a century. *Nat Rev Mol Cell Biol* 2002;**3**:710−8.
2. Lorenz R, Bertinetti D, Herberg F. cAMP-dependent protein kinase and cGMP-dependent protein kinase as cyclic nucleotide effectors. *Handb Exp Pharmacol* 2017;**238**:105−22.
3. Uckert S, Hedlund P, Waldkirch E, Sohn M, Jonas U, Andersson K, et al. Interactions between cGMP- and cAMP-pathways are involved in the regulation of penile smooth muscle tone. *World J Urol* 2004;**22**:261−6.
4. Lafontan M, Moro C, Berlan M, Crampes F, Sengenes C, Galitzky J. Control of lipolysis by natriuretic peptides and cyclic GMP. *Trends Endocrinol Metab* 2008;**19**:130−7.
5. Begonja A, Gambaryan S, Schulze H, Patel-Hett S, Italiano J, Hartwig J, et al. Differential roles of cAMP and cGMP in megakaryocyte maturation and platelet biogenesis. *Exp Hematol* 2013;**41**:91−101.e4.
6. Manoury B, Idres S, Leblais V, Fischmeister R. Ion channels as effectors of cyclic nucleotide pathways: functional relevance for arterial tone regulation. *Pharmacol Ther* 2020;**209**:107499.
7. Beavo J. Cyclic nucleotide phosphodiesterases: functional implications of multiple isoforms. *Physiol Rev* 1995;**75**:725−48.
8. Abdollahi M, Chan T, Subrahmanyam V, O'Brien P. Effects of phosphodiesterase 3,4,5 inhibitors on hepatocyte cAMP levels, glycogenolysis, gluconeogenesis and susceptibility to a mitochondrial toxin. *Mol Cell Biochem* 2003;**252**:205−11.
9. Menniti F, Faraci W, Schmidt C. Phosphodiesterases in the CNS: targets for drug development. *Nat Rev Drug Discov* 2006;**5**:660−70.
10. Kelly M. Cyclic nucleotide signaling changes associated with normal aging and age related diseases of the brain. *Cell Signal* 2018;**42**:281−91.
11. Fujishige K, Kotera J, Michibata H, Yuasa K, Takebayashi S, Okumura K, et al. Cloning and characterization of a novel human phosphodiesterase that hydrolyzes both cAMP and cGMP (PDE10A). *J Biol Chem* 1999;**274**:18438−45.
12. Coskran T, Morton D, Menniti F, Adamowicz W, Kleiman R, Ryan A, et al. Immunohistochemical localization of phosphodiesterase 10A in multiple mammalian species. *J Histochem Cytochem* 2006;**54**:1205−13.
13. Xie Z, Adamowicz W, Eldred W, Jakowski A, Kleiman R, Morton D, et al. Cellular and subcellular localization of PDE10A, a striatum-enriched phosphodiesterase. *Neuroscience* 2006;**139**:597−607.
14. Russwurm C, Koesling D, Russwurm M. Phosphodiesterase 10A is tethered to a synaptic signaling complex in striatum. *J Biol Chem* 2015;**290**:11936−47.
15. Piccart E, De Backer J, Gall D, Lambot L, Raes A, Vanhoof G, et al. Genetic deletion of PDE10A selectively impairs incentive salience attribution and decreases medium spiny neuron excitability. *Behav Brain Res* 2014;**268**:48−54.
16. Schmidt C, Chapin D, Cianfrogna J, Corman M, Hajos M, Harms J, et al. Preclinical characterization of selective phosphodiesterase 10A inhibitors: a new therapeutic approach to the treatment of schizophrenia. *J Pharmacol Exp Therapeut* 2008;**325**:681−90.
17. Kehler J, Nielsen J. PDE10A inhibitors: novel therapeutic drugs for schizophrenia. *Curr Pharmaceut Des* 2011;**17**:137−50.
18. Suzuki K, Harada A, Suzuki H, Miyamoto M, Kimura H. TAK-063, a PDE10A inhibitor with balanced activation of direct and indirect pathways, provides potent antipsychotic-like effects in multiple paradigms. *Neuropsychopharmacology* 2016;**41**:2252−62.
19. Geerts H, Spiros A, Roberts P. Phosphodiesterase 10 inhibitors in clinical development for CNS disorders. *Expert Rev Neurother* 2017;**17**:553−60.

20. Harada A, Suzuki K, Kimura H. TAK-063, a novel phosphodiesterase 10A inhibitor, protects from striatal neurodegeneration and ameliorates behavioral deficits in the R6/2 mouse model of huntington's disease. *J Pharmacol Exp Therapeut* 2017;**360**:75−83.

21. Abdel-Magid AF. Potential of PDE10A inhibitors as treatment for Schizophrenia and other neurological disorders. *ACS Med Chem Lett* 2018;**9**:866−7.

22. Eliwa D, Albadry MA, Ibrahim AS, Kabbash A, Meepagala K, Khan IA, et al. Biotransformation of papaverine and *in silico* docking studies of the metabolites on human phosphodiesterase 10A. *Phytochemistry* 2021;**183**:112598.

23. Kim DY, Park JS, Leem YH, Park JE, Kim HS. The Potent PDE10A inhibitor MP-10 (PF-2545920) suppresses microglial activation in LPS-induced neuroinflammation and MPTP-induced Parkinson's disease mouse models. *J Neuroimmune Pharmacol* 2021;**16**:470−82.

24. Baillie GS, Tejeda GS, Kelly MP. Therapeutic targeting of 3′,5′-cyclic nucleotide phosphodiesterases: inhibition and beyond. *Nat Rev Drug Discov* 2019;**18**:770−96.

25. Walling DP, Banerjee A, Dawra V, Boyer S, Schmidt CJ, DeMartinis N. Phosphodiesterase 10A inhibitor monotherapy is not an effective treatment of acute schizophrenia. *J Clin Psychopharmacol* 2019;**39**:575−82.

26. Yurgelun-Todd DA, Renshaw PF, Goldsmith P, Uz T, Macek TA. A randomized, placebo-controlled, phase 1 study to evaluate the effects of TAK-063 on ketamine-induced changes in fMRI BOLD signal in healthy subjects. *Psychopharmacology* 2020;**237**:317−28.

27. Macek TA, McCue M, Dong X, Hanson E, Goldsmith P, Affinito J, et al. A phase 2, randomized, placebo-controlled study of the efficacy and safety of TAK-063 in subjects with an acute exacerbation of schizophrenia. *Schizophr Res* 2019;**204**:289−94.

28. Sun J, Xiao Z, Haider A, Gebhard C, Xu H, Luo H, et al. Advances in cyclic nucleotide phosphodiesterase-targeted PET imaging and drug discovery. *J Med Chem* 2021;**64**:7083−109.

29. Ahmad R, Bourgeois S, Postnov A, Schmidt M, Bormans G, Van Laere K, et al. PET imaging shows loss of striatal PDE10A in patients with Huntington disease. *Neurology* 2014;**82**:279−81.

30. Boscutti G EAR, Plisson C. PET Radioligands for imaging of the PDE10A in human: current status. *Neurosci Lett* 2019;**691**:11−7.

31. Ahmed H, Haider A, Varisco J, Stankovic M, Wallimann R, Gruber S, et al. Structure−affinity relationships of 2,3,4,5-tetrahydro-1*H*-3-benzazepine and 6,7,8,9-tetrahydro-5*H*-benzo[7]annulen-7-amine analogues and the discovery of a radiofluorinated 2,3,4,5-tetrahydro-1*H*-3-benzazepine congener for imaging GluN2B subunit-containing *N*-methyl-ᴅ-aspartate receptors. *J Med Chem* 2019;**62**:9450−70.

32. Takamura Y, Kakuta H. *In vivo* receptor visualization and evaluation of receptor occupancy with positron emission tomography. *J Med Chem* 2021;**64**:5226−51.

33. Takano A, Stenkrona P, Stepanov V, Amini N, Martinsson S, Tsai M, et al. A human [¹¹C]T-773 PET study of PDE10A binding after oral administration of TAK-063, a PDE10A inhibitor. *Neuroimage* 2016;**141**:10−7.

34. Delnomdedieu M, Forsberg A, Ogden A, Fazio P, Yu C, Stenkrona P, et al. *In vivo* measurement of PDE10A enzyme occupancy by positron emission tomography (PET) following single oral dose administration of PF-02545920 in healthy male subjects. *Neuropharmacology* 2017;**117**:171−81.

35. Tu Z, Fan J, Li S, Jones L, Cui J, Padakanti P, et al. Radiosynthesis and *in vivo* evaluation of [¹¹C]MP-10 as a PET probe for imaging PDE10A in rodent and non-human primate brain. *Bioorg Med Chem* 2011;**19**:1666−73.

36. Plisson C, Weinzimmer D, Jakobsen S, Natesan S, Salinas C, Lin S, et al. Phosphodiesterase 10A PET radioligand development program: from pig to human. *J Nucl Med* 2014;**55**:595−601.

37. Niccolini F, Foltynie T, Reis Marques T, Muhlert N, Tziortzi A, Searle G, et al. Loss of phosphodiesterase 10A expression is associated with progression and severity in Parkinson's disease. *Brain* 2015;**138**:3003−15.

38. Niccolini F, Haider S, Reis Marques T, Muhlert N, Tziortzi A, Searle G, et al. Altered PDE10A expression detectable early before symptomatic onset in Huntington's disease. *Brain* 2015;**138**:3016−29.

39. Marques T, Natesan S, Niccolini F, Politis M, Gunn R, Searle G, et al. Phosphodiesterase 10A in schizophrenia: a PET study using [¹¹C]IMA107. *Am J Psychiatr* 2016;**173**:714−21.

40. Kehler J, Kilburn J, Estrada S, Christensen S, Wall A, Thibblin A, et al. Discovery and development of ¹¹C-Lu AE92686 as a radioligand for PET imaging of phosphodiesterase10A in the brain. *J Nucl Med* 2014;**55**:1513−8.

41. Bodén R, Persson J, Wall A, Lubberink M, Ekselius L, Larsson E, et al. Striatal phosphodiesterase 10A and medial prefrontal cortical thickness in patients with schizophrenia: a PET and MRI study. *Transl Psychiatry* 2017;**7**:e1050.

42. Lin S, Labaree D, Chen M, Holden D, Gallezot J, Kapinos M, et al. Further evaluation of [¹¹C]MP-10 as a radiotracer for phosphodiesterase 10A: PET imaging study in rhesus monkeys and brain tissue metabolite analysis. *Synapse* 2015;**69**:86−95.

43. Celen S, Koole M, De Angelis M, Sannen I, Chitneni S, Alcazar J, et al. Preclinical evaluation of ¹⁸F-JNJ41510417 as a radioligand for PET imaging of phosphodiesterase-10A in the brain. *J Nucl Med* 2010;**51**:1584−91.

44. Andrés J, De Angelis M, Alcázar J, Iturrino L, Langlois X, Dedeurwaerdere S, et al. Synthesis, *in vivo* occupancy, and radiolabeling of potent phosphodiesterase subtype-10 inhibitors as candidates for positron emission tomography imaging. *J Med Chem* 2011;**54**:5820−35.

45. Ooms M, Celen S, Koole M, Langlois X, Schmidt M, De Angelis M, et al. Synthesis and biological evaluation of carbon-11 and fluorine-18 labeled tracers for *in vivo* visualization of PDE10A. *Nucl Med Biol* 2014;**41**:695−704.

46. Stepanov V, Takano A, Nakao R, Amini N, Miura S, Hasui T, et al. Development of two fluorine-18 labeled PET radioligands targeting PDE10A and *in vivo* PET evaluation in nonhuman primates. *Nucl Med Biol* 2018;**57**:12−9.

47. Barret O, Thomae D, Tavares A, Alagille D, Papin C, Waterhouse R, et al. *In vivo* assessment and dosimetry of 2 novel PDE10A PET radiotracers in humans: ¹⁸F-MNI-659 and ¹⁸F-MNI-654. *J Nucl Med* 2014;**55**:1297−304.

48. Russell D, Jennings D, Barret O, Tamagnan G, Carroll V, Caille F, et al. Change in PDE10 across early Huntington disease assessed by [¹⁸F]MNI-659 and PET imaging. *Neurology* 2016;**86**:748−54.

49. Russell D, Barret O, Jennings D, Friedman J, Tamagnan G, Thomae D, et al. The phosphodiesterase 10 positron emission tomography tracer, [¹⁸F]MNI-659, as a novel biomarker for early Huntington disease. *JAMA Neurol* 2014;**71**:1520−8.

50. Mori W, Yamasaki T, Fujinaga M, Ogawa M, Zhang Y, Hatori A, et al. Development of 2-(2-(3-(4-([¹⁸F]fluoromethoxy-*d₂*)phenyl)-7-methyl-4-oxo-3,4-dihydroquinazolin-2-yl)ethyl)-4-isopropoxyisoindoline-1,3-dione for Positron-Emission-Tomography imaging of phosphodiesterase 10A in the brain. *J Med Chem* 2018;**62**:688−98.

51. Cox C, Hostetler E, Flores B, Evelhoch J, Fan H, Gantert L, et al. Discovery of [¹¹C]MK-8193 as a PET tracer to measure target engagement of phosphodiesterase 10A (PDE10A) inhibitors. *Bioorg Med Chem Lett* 2015;**25**:4893−8.

52. Rotstein B, Stephenson N, Vasdev N, Liang SH. Spirocyclic hypervalent iodine(III)-mediated radiofluorination of non-activated and hindered aromatics. *Nat Commun* 2014;**5**:4365.

53. Wang L, Jacobson O, Avdic D, Rotstein B, Weiss I, Collier L, et al. Ortho-stabilized ¹⁸F-azido click agents and their application in PET imaging with single-stranded DNA aptamers. *Angew Chem Int Ed Engl* 2015;**54**:12777−81.

54. Rotstein B, Wang L, Liu R, Patteson J, Kwan E, Vasdev N, et al. Mechanistic studies and radiofluorination of structurally diverse pharmaceuticals with spirocyclic iodonium(III) ylides. *Chem Sci* 2016;**7**:4407−17.

55. Liang S, Wang L, Stephenson N, Rotstein B, Vasdev N. Facile ¹⁸F labeling of non-activated arenes *via* a spirocyclic iodonium(III) ylide method and its application in the synthesis of the mGluR₅ PET radiopharmaceutical [¹⁸F]FPEB. *Nat Protoc* 2019;**14**:1530−45.

56. Ye W, Xie M, Wei J, Li G, Tang Y, Hou L, et al. A fluorinated azine as a versatile scaffold for the development of Cu(II)-specific multi-functional imaging probes. *Sensor Actuator B Chem* 2021;**343**:130106.

57. Takano A, Stepanov V, Gulyás B, Nakao R, Amini N, Miura S, et al. Evaluation of a novel PDE10A PET radioligand, [11C]T-773, in nonhuman primates: brain and whole body PET and brain autoradiography. *Synapse* 2015;**69**:345−55.

58. Wagner S, Teodoro R, Deuther-Conrad W, Kranz M, Scheunemann M, Fischer S, et al. Radiosynthesis and biological evaluation of the new PDE10A radioligand [18F]AQ28A. *J Label Compd Radiopharm* 2017;**60**:36−48.

59. Ory D, Postnov A, Koole M, Celen S, de Laat B, Verbruggen A, et al. Quantification of TSPO overexpression in a rat model of local neuroinflammation induced by intracerebral injection of LPS by the use of [18F]DPA-714 PET. *Eur J Nucl Med Mol Imag* 2016;**43**:163−72.

60. Preshlock S, Tredwell M, Gouverneur V. ^{18}F-Labeling of arenes and heteroarenes for applications in positron emission tomography. *Chem Rev* 2016;**116**:719−66.

61. Targum S, Cara Pendergrass J, Toner C, Zumpano L, Rauh P, DeMartinis N. Impact of BPRS interview length on ratings reliability in a schizophrenia trial. *Eur Neuropsychopharmacol* 2015;**25**:312−8.

62. Lammertsma A, Hume S. Simplified reference tissue model for PET receptor studies. *Neuroimage* 1996;**4**:153−8.

63. Liu H, Jin H, Yue X, Han J, Yang H, Flores H, et al. Comparison of [11C]TZ1964B and [18F]MNI659 for PET imaging brain PDE10A in nonhuman primates. *Pharmacol Res Perspect* 2016;**4**:e00253.

64. Liu H, Jin H, Luo Z, Yue X, Zhang X, Flores H, et al. *In vivo* characterization of two F-labeled PDE10A PET radioligands in nonhuman primate brains. *ACS Chem Neurosci* 2018;**9**:1066−73.

65. Cumberland W, Fong Y, Yu X, Defawe O, Frahm N, De Rosa S. Nonlinear calibration model choice between the four and five-parameter logistic models. *J Biopharm Stat* 2015;**25**:972−83.

66. Hennenberg M, Schott M, Kan A, Keller P, Tamalunas A, Ciotkowska A, et al. Inhibition of adrenergic and non-adrenergic smooth muscle contraction in the human prostate by the phosphodiesterase 10-selective inhibitor TC-E 5005. *Prostate* 2016;**76**:1364−74.

67. Nandhikonda P, Yasgar A, Baranowski A, Sidhu P, McCallum M, Pawlak A, et al. Peroxisome proliferation-activated receptor delta agonist GW0742 interacts weakly with multiple nuclear receptors, including the vitamin D receptor. *Biochemistry* 2013;**52**:4193−203.

68. Jing YR, Zhou W, Li WL, Zhao LX, Wang YF. The synthesis of novel taxoids for oral administration. *Bioorg Med Chem* 2014;**22**:194−203.

69. McLaren DG, Kosmatka KJ, Oakes R, Kroenke CD, Kohama SG, Matochik JA, et al. A population-average MRI-based atlas collection of the rhesus macaque. *Neuroimage* 2009;**45**:52−9.

70. Nie B, Wang L, Hu Y, Liang S, Tan Z, Chai P, et al. A population stereotaxic positron emission tomography brain template for the macaque and its application to ischemic model. *Neuroimage* 2019;**203**:116163.